Sensorimotor beta burst dynamics and interhemispheric connectivity in children with developmental coordination disorder

Holly Rayson[1,2,3*], Sarah A. Gerson[4*], Jennifer Keating[5], Catherine R.G. Jones[4], Catherine Purcell[6], James J Bonaiuto[1,2,3**], Ross E Vanderwert[4,7**]

1) Marc Jeannerod Institute of Cognitive Sciences, ISC, CNRS UMR5229, Lyon, France
2) Université Claude Bernard Lyon 1, Université de Lyon, France
3) Hospices Civils de Lyon, Lyon, France
4) School of Psychology, Cardiff University Centre for Human Developmental Science (CUCHDS), Cardiff, United Kingdom
5) School of Social Sciences, Cardiff University, Cardiff, United Kingdom
6) School of Healthcare Sciences, Cardiff University, Cardiff, UK
7) School of Psychology, Cardiff University Brain Research Imaging Centre (CUBRIC), Cardiff, United Kingdom
* authors contributed equally
** authors contributed equally

Correspondence: Holly Rayson <holly.rayson1@gmail.com>

Keywords: developmental coordination disorder (DCD), sensorimotor activity; beta bursts; functional connectivity; development; interhemispheric connectivity; EEG; beta burst waveforms, Granger causality

Funding: This work was supported by the European Research Council (ERC) under the European Union's Horizon 2020 research and innovation programme (ERC consolidator grant 864550) and British Council Springboard programme (grant 525715).

Abstract

Activity in the beta frequency band appears to play a critical role in various sensorimotor processes, with transient 'bursts' of beta displaying distinct waveform motifs reflecting different neural processes. However, much remains unknown about how beta bursts develop, and hence the role they may play in sensorimotor difficulties associated with neurodevelopmental conditions. Here, we used EEG to investigate sensorimotor beta bursts in children with and without developmental coordination disorder (DCD), which is associated with impaired motor control and atypical brain connectivity. However, the neural dynamics underlying these differences remain unclear. We characterized beta bursts during action execution and observation of gross and fine motor actions. Although overall burst features were similar across groups in the spectral domain, children with DCD showed disrupted rate modulation of specific burst waveform motifs, characterized by atypical lateralization and altered interhemispheric connectivity. These disruptions were strongest for a subset of burst types identified by principal component analysis, and individual differences in motif-specific burst rates correlated with motor ability. Our findings suggest that selective recruitment of distinct beta burst motifs and related

disruption of interhemispheric communication may represent an important mechanism underlying motor difficulties in DCD. This work highlights the importance of burst waveform diversity for understanding typical and atypical motor development.

1. Introduction

Sensorimotor beta activity (13–30 Hz in adults) has long been associated with motor control and is traditionally conceptualized as a sustained oscillatory rhythm that modulates in power prior to, during, and after movement (Pfurtscheller, 1981; Pfurtscheller et al., 1996). However, this view has been challenged by recent demonstrations that beta activity occurs in transient, burst-like events, rather than as a continuous oscillation (Feingold et al., 2015; Sherman et al., 2016; Little et al., 2019). These *beta bursts* are highly dynamic, and appear to play an important role in sensorimotor processing (Shin et al., 2017; Little et al., 2019), including during observation of others' manual actions (Rayson et al., 2023). The latter suggests that beta bursts may also be implicated in motor simulation (Jeannerod, 2001; Press et al., 2011), and the activation of internal models. Until recently, limited research has focused on early development of beta activity, but increasingly, evidence suggests that the beta frequency range shifts with age, that activity in this band occurs in bursts from infancy, and that the timing, duration, and lateralization of these bursts undergo significant changes between infancy and adulthood (Gaetz et al., 2010; Cheyne et al., 2014; Rayson et al., 2022, 2023; Rier et al., 2024; Wilkinson et al., 2024). In adults, beta burst timing and modulation are strong predictors of response time, motor errors, and stopping behavior (Little et al., 2019; Wessel, 2020; West et al., 2023), suggesting that the refinement of beta bursts may be a key component of motor maturation. The functional role of beta bursts in cortical computation and communication is unclear, but developmental changes in beta burst dynamics may provide a critical lens through which to clarify how transient beta events contribute to sensorimotor processing.

Most studies of beta bursts treat them as homogenous neural events, but recent work suggests that this view overlooks their potential functional diversity. Using waveform shape rather than standard time-frequency features such as frequency, power, and duration, beta bursts can be classified into distinct waveform motifs, which are ranges of recurring burst shapes in the raw time-domain signal that capture systematic deviations from the mean burst waveform. These motifs differ in their rate dynamics and lateralization, and accumulating evidence suggests that they index distinct functional processes (Rayson et al., 2023; Szul et al., 2023; Agouram et al., 2025). We recently demonstrated that infant beta bursts share the same basic waveform shape as adults, but they last longer. By accounting for this duration difference, infant bursts can be "warped" in time so that their waveforms align closely with those of adults (Rayson et al., 2023). Infants and adults also share similar patterns of waveform variability around the mean, suggesting that developmental maturation of sensorimotor networks involve progressive refinement of burst waveform motifs. These motifs show distinct patterns of rate modulation that become increasingly precise from infancy to adulthood (Rayson et al., 2023) implying functional specialization across development. Examining beta bursts in populations with atypical motor development, such as developmental coordination

disorder (DCD), a neurodevelopmental condition characterized by persistent difficulties in motor coordination (Wilson et al., 2017), can therefore provide additional critical insights. If different types of beta bursts indeed have specific functional roles in sensorimotor computation and communication throughout development, then examining how their disruption manifests in DCD offers a valuable opportunity to determine their precise contributions to motor control and network organization.

Recent evidence suggests that beta bursts with distinct waveform shapes exhibit different patterns of lateralized rate modulation during movement execution, with some burst motifs becoming increasingly lateralized across early development (Rayson et al., 2023). This pattern of waveform-specific lateralization raises the possibility that certain burst types facilitate interhemispheric sensorimotor communication. DCD is characterized by atypical brain connectivity (Brown-Lum and Zwicker, 2015; Brown-Lum et al., 2020; Subara-Zukic et al., 2022; Van Dyck et al., 2022), reduced hemispheric specialization within sensorimotor networks (Querne et al., 2008; Tallet et al., 2013; McLeod et al., 2016), atypical sensorimotor responses during observation and execution of actions (Keating et al., 2023), and motor deficits including difficulties in motor learning (Bo and Lee, 2013; Subara-Zukic et al., 2022). Given this profile of atypicalities, examining waveform-specific burst dynamics in DCD represents a valuable framework for testing how disruptions in interhemispheric communication might contribute to these differences.

Here, we aimed to characterize sensorimotor beta burst activity in children with and without DCD to determine whether these transient events are altered in children with DCD relative to comparison children during action execution and observation. We show that children with DCD exhibit altered waveform-specific beta burst dynamics, including atypical modulation and lateralization patterns, compared to children without DCD. Specifically, we find that bursts with distinct waveform shapes differ significantly in their lateralized occurrence during movement execution and observation tasks, as well as functional connectivity, suggesting disrupted interhemispheric communication in DCD. These differences correlate with individual variability in motor skill, highlighting a potential neural mechanism underlying motor coordination difficulties in this population.

2. Methods

2.1 Participants

Twenty-three 8- to 12-year-old children with DCD (*M* = 10.88, *SD* = 1.56; 18 male) were recruited via social media and the Dyspraxia Foundation, and 33 typically developing children (*M* = 9.85, *SD* = 1.30; 17 male) were recruited via social media as a comparison group. Participants in the DCD group were required to have received a clinical diagnosis of DCD, confirmed for this study via parent report and converted total score on the Movement Assessment Battery for Children 2nd Edition (MABC-2; Henderson et al., 2007) at or below the 16th percentile at the time of the testing session.

In line with the Leeds Consensus Statement (2006), participants with a diagnosis of DCD who had co-occurring neurodevelopmental conditions were not excluded from participating, but additional diagnoses were noted. In the final sample, co-occurring conditions were autism (n = 3), ADHD (n = 1), dyslexia (n = 1), and autism, dyslexia, developmental language disorder and learning difficulty (n = 1). Children were not recruited to the comparison group if they had a diagnosis of a neurodevelopmental condition or developmental delay.

Nine children from the comparison group were excluded from the analyses of group differences as they scored below the 25th percentile on the MABC-2. This was to ensure we were not including children in the comparison group who did not have normative motor development (French et al., 2018). A further six participants were excluded during EEG processing due to insufficient data (DCD n = 4; comparison n = 2). The final sample therefore included 19 children with DCD (M_{age} = 11.17 years, SD = 1.28; 14 male; 14 right-handed) and 22 children without DCD (M_{age} = 9.78 years, SD = 1.40; 12 male; 21 right-handed). Full testing and demographic details are available in Keating et al., (2023); however we note here that the comparison group had significantly higher IQ scores (p = .011) (assessed by the Weschler Abbreviated Scales of Intelligence, 2nd edition [WASI-II]; Weschler, 2011) and were significantly younger than the DCD group (p = .002). Written informed consent was obtained from the participant's caregiver before the start of the experiment. Each child also provided written assent to take part. Ethical approval was granted by the Ethics Committee at BLINDED FOR REVIEW. Participants received travel expenses and a small prize.

2.2 Movement Assessment Battery for Children

The Movement Assessment Battery for Children 2nd Edition (MABC-2; Henderson et al., 2007) test component was used to assess motor skills. The MABC-2 has good internal consistency and test re-test reliability (Henderson et al., 2007; Wuang et al., 2012). The assessment consists of eight tasks organized into three subsets: manual dexterity, aiming and catching, and static and dynamic balance. Age-adjusted standard scores were calculated for each subtest, and a total difficulty score was created from which percentiles can be derived. A total score below the 5th percentile indicates significant motor difficulties, a score between the 5th and 16th percentile indicates a risk of motor difficulties, and a score above the 25th percentile indicates age-expected motor ability.

2.3 Task and Stimuli

Video stimuli for the EEG motor tasks were filmed using a handheld camera fixed to a tripod. The camera was positioned overlooking the model's shoulder while she performed the actions to best match the participant's perspective of the actions as if they were performing them, while also providing a clear view of the entire action. We chose an

ego-centric perspective because previous studies have suggested this elicits greater sensorimotor activity (Jackson et al., 2006; Fu and Franz, 2014; Drew et al., 2015).

All videos were trimmed to fit within a 10-second period, with three types of videos in total (gross motor, fine motor, and non-biological movement). The gross motor video displayed a model sitting with the hand starting at rest on the edge of a table, extending the arm to reach out and tap a red square, and then returning the arm to rest. This action took approximately 2 seconds and was repeated 5 times. The fine motor video displayed a hand holding a red pen and tracing a flower figure (based on the Movement Assessment Battery for Children; Henderson et al., 1992). The tracing lasted approximately 20 seconds and was split into two separate videos; therefore, half of the fine motor action observation trials began with an empty flower and showed the hand tracing halfway around and the other half began with the hand already halfway around the flower and continued tracing to the end of the flower. The non-biological movement videos were of kaleidoscope patterns taken from Pixabay (www.pixabay.com). All videos of actions were performed by a right-handed person and were mirrored to make the actions appear to be performed by a left-handed model for left-handed participants (n = 6). All videos were presented on the center of the screen, subtending a visual angle of ~28° (horizontal) and ~14° (vertical). Example stimuli are displayed in Figure 1 and are available at https://osf.io/vnup9/.

The EEG task consisted of five conditions adapted from Hobson and Bishop (2016; Figure 1). Two conditions were execution trials: Execution Gross motor (ExG) and Execution Fine motor (ExF). These began with an instruction screen describing the action with an image of the action stimulus (i.e. a red square for ExG/the flower for ExF). Once the participant was ready, the experimenter initiated the trial with a button press. During the trial, the command ‘GO’ was displayed beneath the action stimulus for 10 seconds while participants performed the action. A ‘STOP’ command was then displayed for 2 seconds. Three conditions consisted of observation trials using the videos described above. These began with a fixation cross. Once the participant was ready, the experimenter initiated the trial with a button press. During the trial, either the Observation Gross motor (ObG), Observation Fine motor (ObF), or the non-biological movement (kaleidoscope; Kal) video played for 10 seconds. Participants completed 40 trials of each condition split across two blocks. Trials were presented in a random order and timing was controlled by E-Prime 3.0 software (Psychology Software Tools).

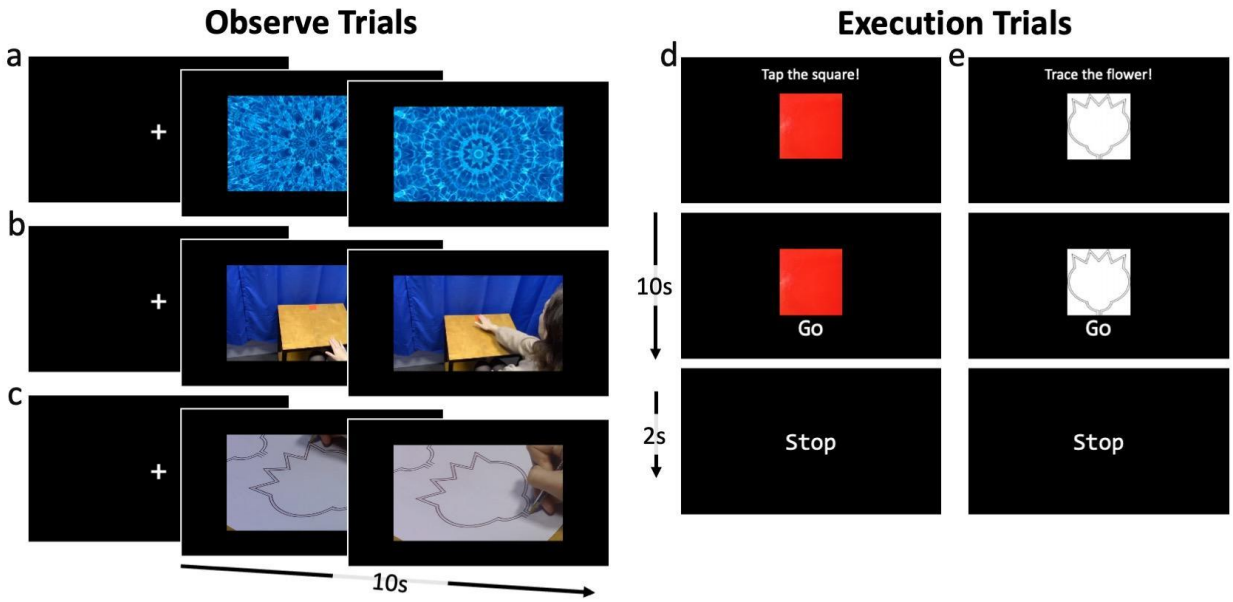

Figure 1. Example Trials in the EEG Task. Observe trials began with a fixation cross to cue participants to remain still and observe the videos for 10 seconds. Example screenshots of the videos are shown for Kaleidoscope (a); the hand reaching for the red square for Gross Motor (b); and a hand tracing a flower for Fine Motor (c) trials. Execution trials began with action instructions to prepare participants; specifically to "Tap the square!" for Gross Motor (d) or "Trace the flower!" for Fine Motor (e) trials. The "Go" screen was then displayed for 10 seconds to initiate participants execution and then the "Stop" screen was displayed for 2 seconds to end the trial.

2.4 Procedure

Each child was prepared for the EEG acquisition, including placement of the EEG cap and preparation of electrodes with electrogel, and then brought into the testing room. Their caregiver was invited to observe the testing session from an adjoining room while they completed questionnaires on a tablet computer (see Keating et al., 2023 for details). During placement of the EEG cap, the child completed the Edinburgh Handedness Inventory – Short Form (Veale, 2014) to determine whether they were dominantly left- or right-handed. Once the EEG was fully set-up, the task was explained to the participant.

Participants sat at a table with a red square affixed to the surface across from a 17" computer screen approximately 80 cm away. The session began by measuring resting-state EEG as the child sat with their eyes first open for 30 seconds, and then their eyes closed for 30 seconds. This procedure was repeated three times.

Following resting measures, children practiced the tasks via completion of two observation trials (one ObG and one ObF) and two execution trials (one ExG and one ExF). Participants then completed the motor task, with the entire session lasting around 25 minutes. Once the EEG session was complete, the EEG cap was removed, and the participants completed the MABC-2 and WASI-II (in this fixed order). Children could take

breaks during testing as needed, with the whole session lasting approximately 100 minutes.

2.5 EEG Acquisition

Continuous EEG was recorded with the BrainVision actiCHamp Plus system (Brain Products GmbH, Gilching, Germany) from 32 channels placed according to the International 10-20 System, and referenced online to the vertex electrode (Cz). ECI Electro-Gel (GVB geliMED GmbH, Germany) was used to reduce impedances, which were kept below 20 kΩ. Data were sampled at 500 Hz. Video recordings of all EEG sessions were coded to identify trials in which participants were not watching a video or completing the required action. Any trials where participants were visibly not attending or were making off-task movements were removed prior to analysis (Observation: *Mdn* = 4, range 0 – 13 trials; Execution: *Mdn* = 2, range 0 – 8 trials).

2.6 Data preprocessing

The EEG data were preprocessed using MATLAB R2018a with a custom version of the MADE pipeline (Debnath et al., 2020), modified to include artifact detection routines from the NEAR pipeline (Kumaravel et al., 2022). The data were first high pass filtered at 1 Hz and low pass filtered at 100 Hz using EEGLAB version 2021.1 (Delorme and Makeig, 2004) FIR filters. Channels with excessive artifacts were identified and removed using the local outlier factor metric from the NEAR pipeline, with an adaptive threshold starting at 4.5 for outlier detection (comparison: 0 - 3 channels, *M* = 0.24, *SD* = 0.66; DCD: 0 - 12 channels, *M* = 0.70, *SD* = 2.51). Artifact subspace reconstruction was then used to identify and correct non-stereotyped artifacts. Stereotyped artifacts such as eye blinks were then detected and removed using the independent component analysis (ICA)-based procedure from the MADE pipeline on a copy of the dataset, which was first segmented into 1 s epochs. Noisy epochs in the copied dataset were removed using a voltage threshold of ±1000 µV. After ICA decomposition, independent components (ICs) were transferred from the copied dataset to the original dataset. Artifactual ICs were removed from the original dataset using the EEGLAB Adjusted-ADJUST plugin, with default values for blink identification thresholds, and alpha peak detection parameters (Mognon et al., 2011; Leach et al., 2020) (comparison: 1 - 19 components, *M* = 8.00, *SD* = 4.73; DCD: 1 - 14 components, *M* = 7.78, *SD* = 2.88). The data were then segmented into 10-s-long epochs, bounded by the start and end of trials in the KaI, ObF, ObG, ExF, and ExG conditions. A voltage threshold of ±150 µV was used to detect artifacts in each channel during each epoch. Epochs in which >10% of the channels contained artifacts were removed (comparison: 0 - 90 epochs, *M* = 23.67, *SD* = 22.51; DCD: 6 - 87 epochs, *M* = 24.91, *SD* = 22.00); otherwise, the artifacted channels were removed and interpolated for that epoch. After artifact rejection, any remaining missing channels were interpolated, and the data were average re-referenced. Finally, line noise (50 Hz) was removed using an iterative version of the Zapline algorithm (de Cheveigné, 2020) implemented in the

MEEGKit package (https://nbara.github.io/python-meegkit/), using a window size of 10 Hz for polynomial fitting and 2.5 Hz for noise peak removal and interpolation. Participants with fewer than 10 trials for a condition were excluded from analysis of that condition. All source code for preprocessing is available at https://github.com/danclab/dcd_bursts/tree/main/preprocessing.

2.7 Beta Burst Detection Algorithm

Burst detection and analysis were focused on the C3 and C4 electrodes (i.e., over left and right sensorimotor cortex), as these are the primary locations of movement-related changes in beta power (Pfurtscheller, 1981; Pfurtscheller et al., 1996). To determine the frequency limits of the beta band, we computed power spectral densities (PSDs) from all data for each participant from 0.1 to 100 Hz using Welch's method with 1-second Hann windows, 50% overlap, and 10 times oversampling. These PSDs were parameterized using specparam (Donoghue et al., 2020) to decompose them into periodic and aperiodic spectral components. The periodic component was averaged over the C3 and C4 electrodes and across participants within each group. Group-level periodic spectral peaks were identified by iteratively fitting a Gaussian function to the global periodic power maximum and subtracting it from the periodic PSD. This process was repeated until no additional peaks were detected. Peak frequency bands were defined by computing the full width at half maximum (FWHM) of each peak, retaining only peaks with a FWHM of at least 2 Hz for those below 10 Hz, or a FWHM of at least 3 Hz for those above 10 Hz. We took the minimum band limit across groups (14 Hz) and the maximum (32 Hz) as the beta band range for burst detection.

Beta bursts were identified using a recently developed adaptive burst detection algorithm (Rayson et al., 2023; Szul et al., 2023), which identifies all potential burst events over a wide range of amplitudes, without the use of a fixed, global threshold. The algorithm works iteratively on individual trial TF decompositions by fitting a 2D Gaussian to the global maxima, subtracting the fitted Gaussian from the TF decomposition, and proceeding with the global maxima of the resulting residual, continuing until no additional bursts are found in the trial. TF decomposition was carried out using the superlet transform (Moca et al., 2021), which optimally balances time and frequency resolution, and is thus particularly suited for detecting transient bursts within narrow frequency bands. An adaptive superlet transform was used, with varying central frequencies (1–50 Hz) and a fixed number of cycles (4 cycles) within a Gaussian envelope. The wavelet order (i.e., the multiplier for the number of cycles in the wavelet) varied linearly from 1 to 40 over the frequency range. PSDs were computed from the TF decomposition for each channel by averaging the TF power over time for individual trials, and subsequently, across trials. The specparam algorithm (Donoghue et al., 2020) was then applied to parameterize the PSD for each channel, estimating and subtracting the aperiodic spectrum from each individual trial TF decomposition. The iterative burst detection

process was then applied to the residual amplitude (Brady and Bardouille, 2022), identifying the global maximum within the TF space, and fitting a 2D Gaussian to this peak. The Gaussian parametrization characterizes burst features in the TF domain, including peak time, duration, peak amplitude, peak frequency, and frequency span. The Gaussian is then subtracted from the TF decomposition, and the next iteration proceeds with the resulting residual TF matrix. The process stops when no peaks exceed the noise floor, which was defined as 2 SDs above the average power across all time and frequency bins, recalculated in every iteration. To minimize edge effects, burst detection was run on TF data in the 11–35 Hz range, and only bursts with peak frequencies within the identified beta band (14–32 Hz) were retained for additional analysis.

We extracted the waveform for each detected burst from the "raw" time series (unfiltered, except for the 100 Hz low-pass filter and 1 Hz high-pass filter applied as part of the data preprocessing). The time window for waveform extraction was 260 ms (Szul et al., 2023), centered on the bust peak time. To identify the signal deflection corresponding to the peak amplitude, we aligned the burst waveforms by band-pass filtering them within their detected frequency span, computing the instantaneous phase using the Hilbert transform, and re-centering the “raw” waveform (before band pass filtering) around the phase minimum closest to the peak time in TF space (Boto et al., 2022). If the time point deviated by more than 30 ms from the TF-detected peak time, the burst was excluded. Finally, the DC offset was removed from the resulting waveform. Code for the burst detection algorithm can be found at https://github.com/danclab/burst_detection.

2.8 Burst analysis

We first compared beta burst features (duration, peak amplitude, peak frequency, and frequency span) and overall burst rate in each experimental condition (Kal, ObF, ObG, ExF, ExG) between the comparison group and the DCD group, in order to confirm that any group differences were not driven by conventional time-frequency measures, which are the features most commonly examined in prior work. To assess statistical significance, we employed a permutation test (N = 100,000), randomly shuffling group labels and comparing the observed difference in mean feature values or burst rate against this null distribution. Burst rates were computed in 0.1 s bins over a 10 s trial window, normalized by the number of trials. Outliers were identified and removed if burst rate values exceeded ±2.5 standard deviations from the mean, computed separately within each PC quartile and condition (and separately by hemisphere in the lateralized analysis). Burst rates in the Ob and Ex conditions were expressed as percentage change relative to the Kal baseline. We first confirmed that there were no group differences in Kal burst rates in the beta range, making it appropriate to use this condition as a subject-specific baseline when comparing groups.

We then used Principal Component Analysis (PCA) with 20 components (Pedregosa et al., 2011) to examine waveform variability and distinguish burst waveform shapes between the comparison and DCD groups. Unlike conventional time-frequency features (e.g., peak frequency, amplitude), which are derived from Fourier decomposition of the time series, waveform analysis focuses on the raw time-domain shape of each detected burst. Burst waveforms were extracted directly during the burst detection algorithm, and PCA was then applied to all bursts pooled across conditions to characterize the full space of waveform variability. We first conducted separate PCAs on each group's burst waveforms (after robust scaling), treating each time point as a feature and representing the mean burst waveform as the origin of a 20-dimensional space. Each burst's waveform was then defined by its scores for each of the principal components (PCs), indicating how it differed from the average waveform along the dimension that defined that component. To determine whether the pattern of waveform variability around the mean was similar between groups, we compared the PCA eigenvectors using Spearman correlation, revealing high consistency in waveform shapes across the two groups. We therefore fit a single PCA to all burst waveforms from both groups, allowing them to be compared within the same representational space.

To identify which PCs captured meaningful variance in the beta burst waveform data, we compared the variance explained by each component of the PCA applied to the real data with the variance distributions from 100 iterations of shuffled data, where rows of each feature column (time points) were randomly permuted to remove temporal correlations (Vieira, 2012). P-values were calculated as the proportion of shuffled PCA results with lower explained variance than the original data. A Bonferroni correction (α = 0.0025) was applied to account for multiple comparisons, identifying PCs 1–11 as meaningful for further analysis.

We identified waveform motifs that were modulated by comparing bursts at baseline (Kal) to those in observation and execution conditions. For each PC, we computed the mean difference in PC scores between baseline and the combined set of conditions (ObF, ObG, ExF, ExG), averaged across participants. We then conducted a permutation test (N = 1,000) in which baseline and condition scores were shuffled to form a null distribution of score differences. PCs whose observed differences exceeded the 95th percentile of this null distribution were deemed significant. These PCs reflected systematic deviations in waveform shape from the baseline, such as shifts in key peaks or troughs. Because changes in mean PC scores can also arise from altered burst occurrence rather than just shape variability, we further analyzed the waveform-specific burst-rates.

For each PC that exhibited significant task-related changes in waveform shape, we sorted bursts into four bins (quartiles 1–4) according to their PC scores. Within each

bin, burst rates were computed by taking the peak times from the relevant condition (e.g., ObF or ExG), binning them in 50 ms intervals, and normalizing by the number of trials. The resulting rates were expressed as a percent change from baseline (the burst rate of the same quartile in the Kal condition), and outliers (> 2.5 SDs from the mean) were removed. Statistical significance was evaluated via a permutation test comparing the comparison group to the DCD group for each PC bin (N = 100,000). In order to determine if PC-defined waveform motifs differed between hemispheres and groups, we then repeated this procedure after splitting bursts by electrode site (C3 or C4) and labeling them as either contralateral or ipsilateral according to each participant's dominant hand. Statistical significance was assessed using both a permutation test (N = 100,000) and a paired bootstrap test (N = 1,000), depending on the specific comparison.

Burst rates were analyzed using linear mixed-effects models to assess differences across groups, conditions, and hemispheres. In the first set of models, burst rate was modeled as a function of group (DCD, comparison) and condition (ObF, ObG, ExF, ExG), with participant as a random intercept. In the second set of models, hemisphere (contralateral, ipsilateral) was added as a fixed effect, and condition was modeled as a random slope within participants. Each model was fit separately for each PC quartile bin. Statistical significance of fixed effects was assessed using Type III Wald χ^2 tests (car v3.1.0; Fox et al., 2019). Pairwise post hoc comparisons were conducted using Tukey-corrected estimated marginal means (lsmeans v2.30; Lenth et al., 2020). Model fitting was performed in R (v4.2.2; R Core Team, 2022) using the lme4 package (v1.1.30; Bates et al., 2014).

2.9 Correlation Analysis with MABC-2 Scores

To evaluate whether the occurrence of specific beta burst waveform motifs was associated with motor coordination, we computed the average burst rate within each PC quartile (1-4) for each participant. Rates were collapsed across all task conditions and electrode hemispheres. Spearman correlations were used to assess the association between burst rate and MABC-2 percentile scores. To supplement these non-parametric results, we fit linear regression models and generated 95% confidence intervals for the regression lines using nonparametric bootstrapping (10,000 iterations, resampling participants with replacement). Outliers (> 2.5 SDs from the mean burst rate within each quartile) were removed prior to analysis.

2.10 Granger Causality Analysis

After examining group differences in burst dynamics along waveform motifs, we assessed directed functional connectivity between ipsilateral and contralateral sensorimotor bursts across four PC quartile bins (Q1–Q4). Burst events were binned in 5 ms intervals over a 10 s window, separately for each participant and channel, and pooled across all task conditions (ObF, ObG, ExF, ExG). For each source-target pair and

quartile, we fitted a Granger causality (GC) model using a negative binomial generalized linear model (GLM) with constant dispersion (α = 1.0), adapted from point process methods (Kim et al., 2011; Agouram et al., 2025). GC was computed by comparing full models (including the lagged activity of a source electrode) against reduced models (with the source term omitted). GC strength was defined as the difference in log-likelihood between these models, and signed according to the coefficient of the source term in the full model. Each model was conditioned on the past activity of all other electrodes, yielding fully conditional GC estimates. Optimal time lags (5–50 ms) for each source–target pair were selected via 10-fold cross-validation, maximizing held-out log-likelihood. Diagonal (within-electrode) GC estimates were excluded due to refractoriness in burst detection, and only inter-hemispheric connections were analyzed. To assess statistical significance, we performed a one-sample permutation test (N = 1,000) by comparing observed GC values to null distributions generated via random trial shuffling within PC quartile and channel, thereby preserving burst statistics while disrupting temporal relationships between hemispheres. For each source–target pair, a p-value was computed as the proportion of permuted GC values exceeding the observed value. These p-values were then corrected for multiple comparisons using the Benjamini-Hochberg false discovery rate (FDR) procedure (α = 0.05), and only FDR-significant GC values were retained for interpretation.

Source code for all of these analyses is available at https://github.com/danclab/dcd_bursts.

3. Results

3.1 Time-frequency-based burst features do not differ between DCD and comparison groups

We used a recently developed iterative algorithm to identify all potential beta burst events (Rayson et al., 2023; Szul et al., 2023). We then compared beta bursts between the comparison and DCD groups in terms of time-frequency-based features and overall burst rate, pooling together bursts detected over the left and right sensorimotor cortex (C3 and C4 electrodes). This revealed no overall differences in these burst features between groups in terms of duration ($M_{comparison}$ = 420.03, *SD* = 49.21 ms; M_{DCD} = 419.91, *SD* = 56.40 ms, p = 0.994; Figure 2a), peak amplitude ($M_{comparison}$ = 0.95, *SD* = 0.32 μV; M_{DCD} = 0.95, *SD* = 0.50 μV; p = 0.962; Figure 2b), peak frequency ($M_{comparison}$ = 19.58, *SD* = 1.12 Hz; M_{DCD} = 19.75, *SD* = 1.41 Hz; p = 0.659; Figure 2c), or frequency span ($M_{comparison}$ = 1.47, *SD* = 0.10 Hz; M_{DCD} = 1.46, *SD* = 0.12 Hz; p = 0.776; Figure 2d). We then examined overall burst rate in the observation (ObF and ObG), and execution (ExF and ExG) conditions, expressed relative to the Kal baseline (which did not differ between groups), and found no group differences in any condition (all p > 0.15).

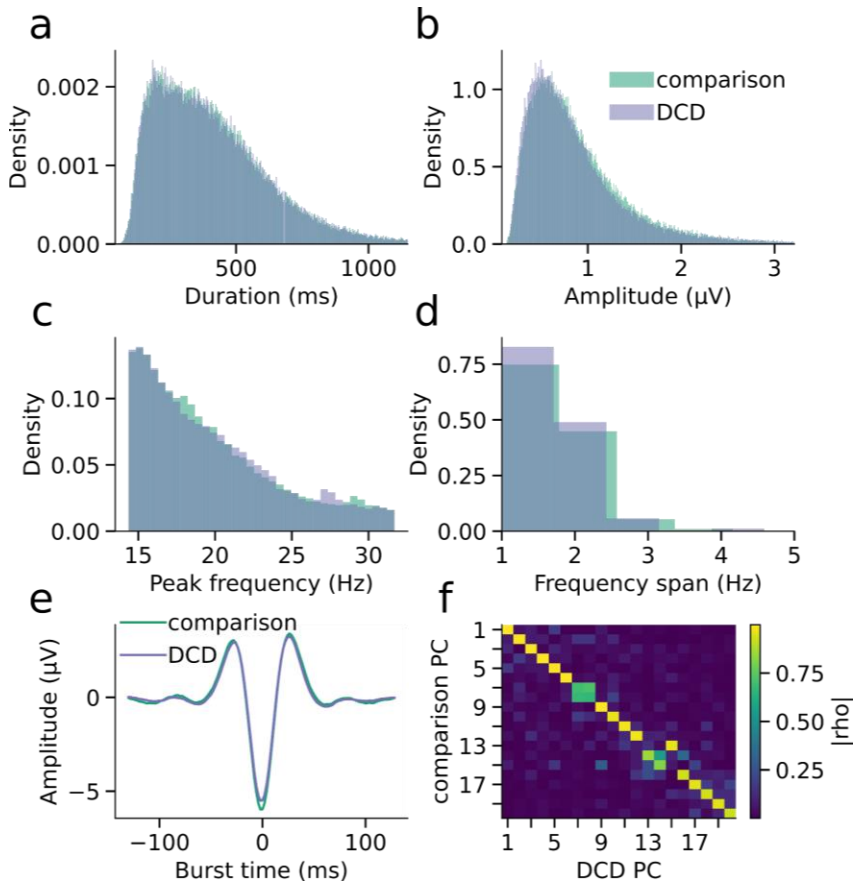

Figure 2. Time frequency -based and waveform features do not differ between groups. Duration (a), amplitude (b), peak frequency (c), and frequency span (d) of sensorimotor cortical bursts in the comparison and DCD groups. e). Median burst waveforms in both groups. f) Absolute value of the correlation coefficient between eigenvectors from the PCA ran only on bursts from the comparison group, and those from the PCA ran only on bursts from the DCD group.

3.2 Sensorimotor cortical bursts share similar waveform motifs across groups

Because time-frequency-based beta burst features are derived from time-frequency decomposition of the burst event time series, and the correspondence between temporal and time-frequency-based burst features is not one-to-one (Jones, 2016; Szul et al., 2023), we then focused our analysis on burst waveform shapes. In line with previous work, we found that sensorimotor cortical bursts in both groups had a wavelet-like median waveform shape with a strong central negative deflection and surrounding positive deflections (Figure 2e; Sherman et al., 2016; Bonaiuto et al., 2021; Brady and Bardouille, 2022; Rayson et al., 2023; Szul et al., 2023). To assess group differences in burst waveform shape, we next applied PCA to the burst waveforms, an approach previously shown to capture functionally relevant waveform motifs (Rayson et al., 2023; Szul et al., 2023). We ran separate PCAs on burst waveforms from each group and compared the resulting eigenvectors. All PCs were highly similar between groups (ρ = 0.68 - 1.0; Figure 2f). For nearly all PCs, the most similar component from the comparison group PCA was the corresponding one of the DCD group PCA, indicating that the

waveform motif and relative percentage of variance explained was very similar across groups. While the overall PC ordering was preserved across groups, the correspondence for PCs 7 and 8 was slightly weaker (ρ_{PC7} = 0.72, ρ_{PC8} = 0.68), suggesting modest group differences in the waveform variability captured along these dimensions.

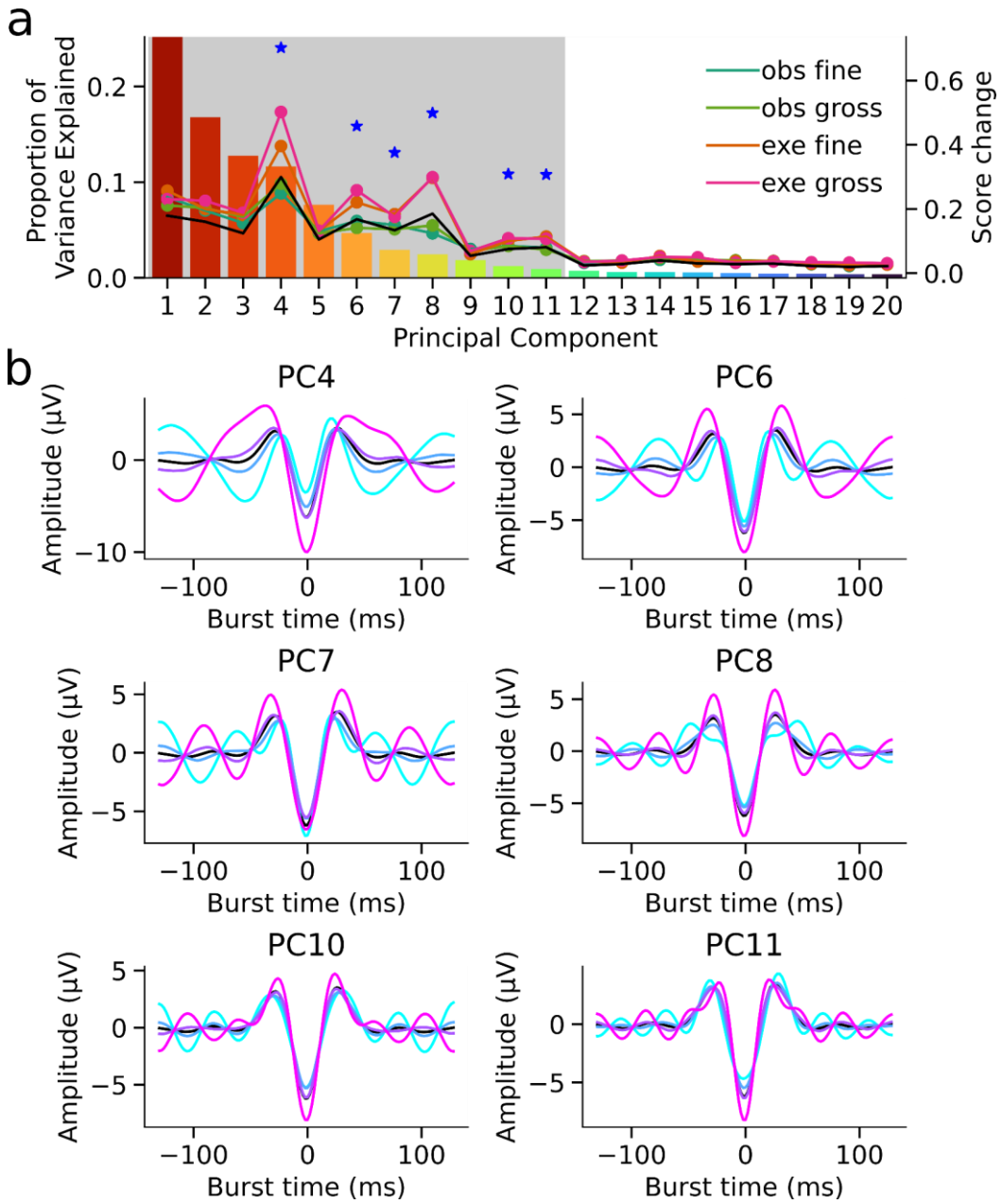

Figure 3. PCA reveals a variety of burst waveform motifs modulated by action observation and execution. a) The histogram shows the proportion of the variance explained by each component. The grey shaded region shows the meaningful components identified by the waveform shuffling permutation analysis. The colored lines overlaid on top of the histogram shows the mean absolute change in score from baseline for each condition (black line shows the global average). The blue stars indicate the PCs which exhibited significant changes in score in the experimental conditions compared to the baseline condition.

b) For each significant component, mean burst waveform shapes of bursts with a score within each quartile of all burst scores for that component (colored lines), compared to the overall mean burst waveform (black).

3.3 Specific burst waveform motifs are modulated by observation and execution tasks

Given the similarity in waveform shape and variability between comparison and DCD group bursts, we then applied a single global PCA to all sensorimotor burst waveforms to analyze them within a common set of dimensions. PCs 1-11 were selected for further analysis based on a permutation test in which the waveforms were temporally shuffled, revealing which components contributed significantly to waveform variability ($p < 0.001$; Figure 3a). To determine which waveform motifs were modulated by the experimental conditions, we then computed the difference in mean burst scores between the observation/execution conditions (ObF, ObG, ExF, ExG) and the baseline condition (Kal), averaged over participants. A permutation test, performed by shuffling the condition labels, identified PCs 4, 6-8, 10, and 11 as those capturing significant differences from baseline in waveform shape ($p < 0.001$). Each of these components defined dimensions along which the waveform shape deviated from the mean waveform (Figure 3b), either in terms of the central negative deflection, the peaks surrounding it, or the additional peripheral peaks. Because a change in mean PC score is ambiguous with respect to the underlying burst rate (i.e. an increase in mean score could be indicative of an increase in occurrence of bursts with high scores, or a decrease in bursts with low scores), these PCs were therefore analysed further in terms of waveform-specific burst rate.

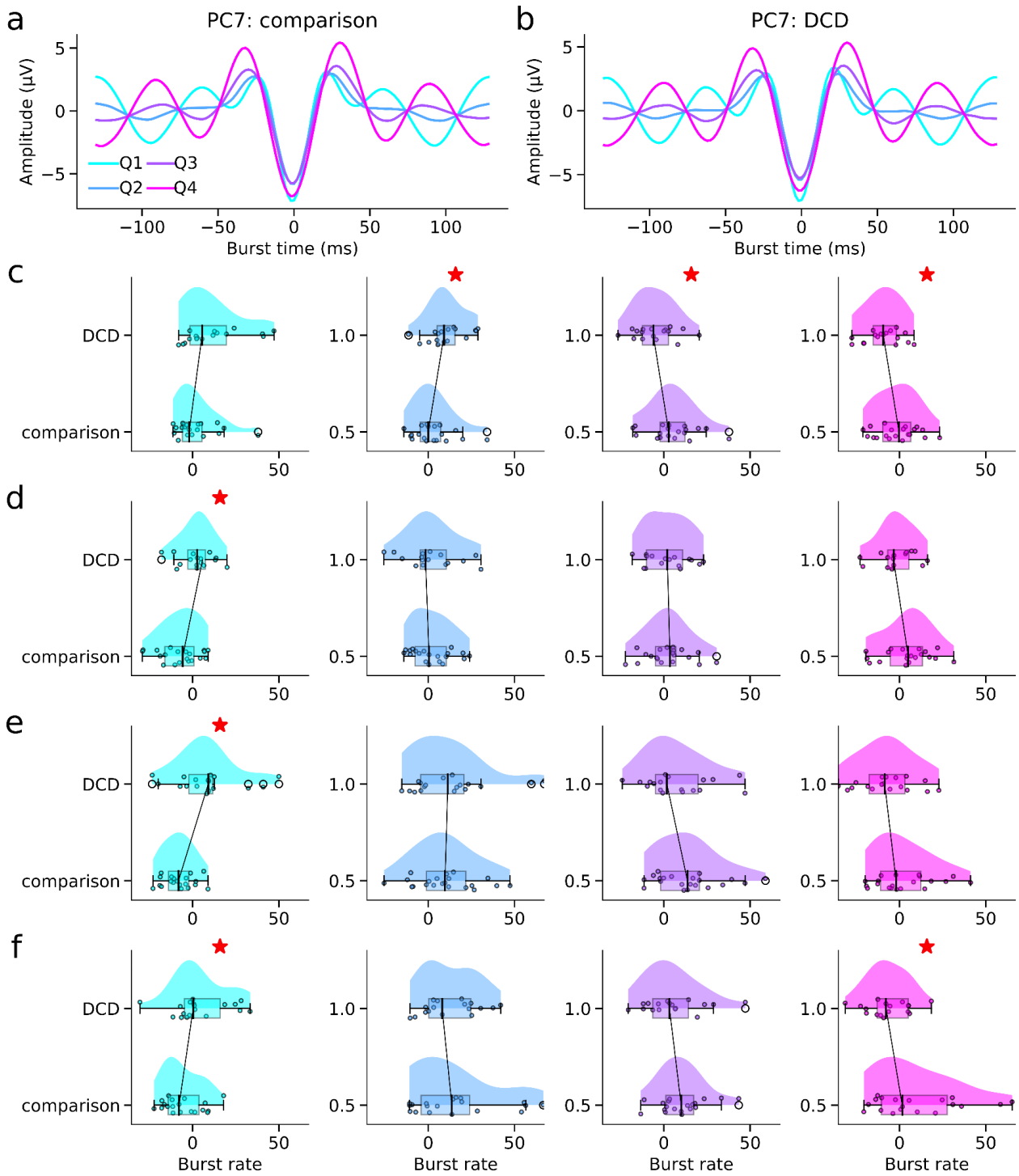

Figure 4. Comparison and DCD groups differ in terms of waveform-specific burst rates along PC7. a) Mean burst waveform shapes of bursts from the comparison group with a score within the first (cyan), second, third, and fourth (magenta) quartile of all burst scores for PC7. b) As in a, for bursts from the DCD group. e-g) Mean burst rate for each group for the (from left to right) first, second, third, and fourth quartiles of PC7 during the ObF (c), ObG (d), ExF (e), and ExG (f) conditions. Points represent individual subjects. Solid lines link median values between groups. Red stars indicate significant differences between groups.

3.4 Waveform-specific burst rates differ between DCD and comparison groups

For each of the PCs defining dimensions along which burst waveform shape during the observation/execution conditions significantly deviated from the baseline condition, we binned all sensorimotor bursts (pooling across hemispheres) into quartiles based on their score along that dimension, as well as the time during the epoch in which they occurred. For each condition, we then computed the burst rate for each PC score quartile (for the ObF, ObG, ExF, and ExG conditions this was computed relative to the baseline condition), and used permutation tests to determine significant differences between the comparison and DCD groups. This analysis revealed a consistent pattern along PC7: children with DCD showed elevated rates of bursts in the first quartile and reduced rates in the fourth quartile compared to the comparison group, and this was significant for the first quartile in the ObG, ExF, and ExG conditions, and in the fourth quartile during the ObF and ExG conditions (Figure 4; Table S1). Additional group differences were observed in the second and third quartiles of PCs 7 in the ObF condition, and the fourth quartile of PC8 in the execution conditions (Figure S1; Table S1).

Given the difference between groups along PC7 across all conditions, we focused subsequent analysis on that component. For each quartile of PC7, we then followed up this permutation-based approach with a linear mixed model analysis of burst rate with group, condition, and their interaction as fixed effects, and subject-specific intercepts as random effects. In line with the permutation test results, this revealed main effects of group for the first quartile of PC 7 ($\chi^2(1) = 13.42$, $p < 0.00$), with a greater rate in the DCD group across conditions ($M_{DCD} = 6.69$, $SD = 16.08$ %, $M_{comparison} = -4.80$, $SD = 11.60$ %). There was a main effect of condition for the third quartile ($\chi^2(3) = 8.82$, $p = 0.03$), with a higher rate during the ExF condition than during both the ObF ($M_{ExF} = 11.27$, $SD = 19.17$ %, $M_{ObF} = 0.27$, $SD = 13.84$ %; $t(106) = 3.67$, $p = 0.00$) and ObG ($M_{ObG} = 2.15$, $SD = 12.77$ %; $t(106) = 2.73$, $p = 0.037$) conditions. Across observation and execution conditions, the DCD group exhibited a consistent redistribution of bursts along PC7, with elevated rates of first-quartile bursts and reduced rates of fourth quartile bursts relative to the comparison group.

3.5 Differences in waveform-specific burst rates along PC7 correlate with motor skill

Having demonstrated a consistent difference in waveform-specific burst rates along PC7 between groups, we next sought to determine if there was a relation between these rates during the observation and execution conditions and motor skill. For this analysis we included the comparison group participants who were excluded from the previous analyses due to having an MABC-2 score below the 25th percentile to be inclusive of variability across the entire sample. Consistent with the group differences in burst rates, there was a negative correlation between the rate of bursts in the first quartile of PC7 during the ObF and ExF conditions and MABC-2 score (ObF: $\rho = -0.32$, $p = 0.041$;

ExF: ρ = -0.49, p = 0.001), and a positive correlation between third and fourth quartile burst rate and MABC-2 score during ObF (third quartile: ρ = 0.34, p = 0.026; fourth quartile: ρ = 0.34, p = 0.028; Figure 5). There was also a negative correlation between the rate of bursts in the second quartile during the ObF condition and MABC-2 score (ρ = -0.41, p = 0.008; Figure 5a). Importantly, the slopes for each quartile were consistently signed across observation and execution conditions, suggesting a generalized relationship between burst rate and motor coordination.

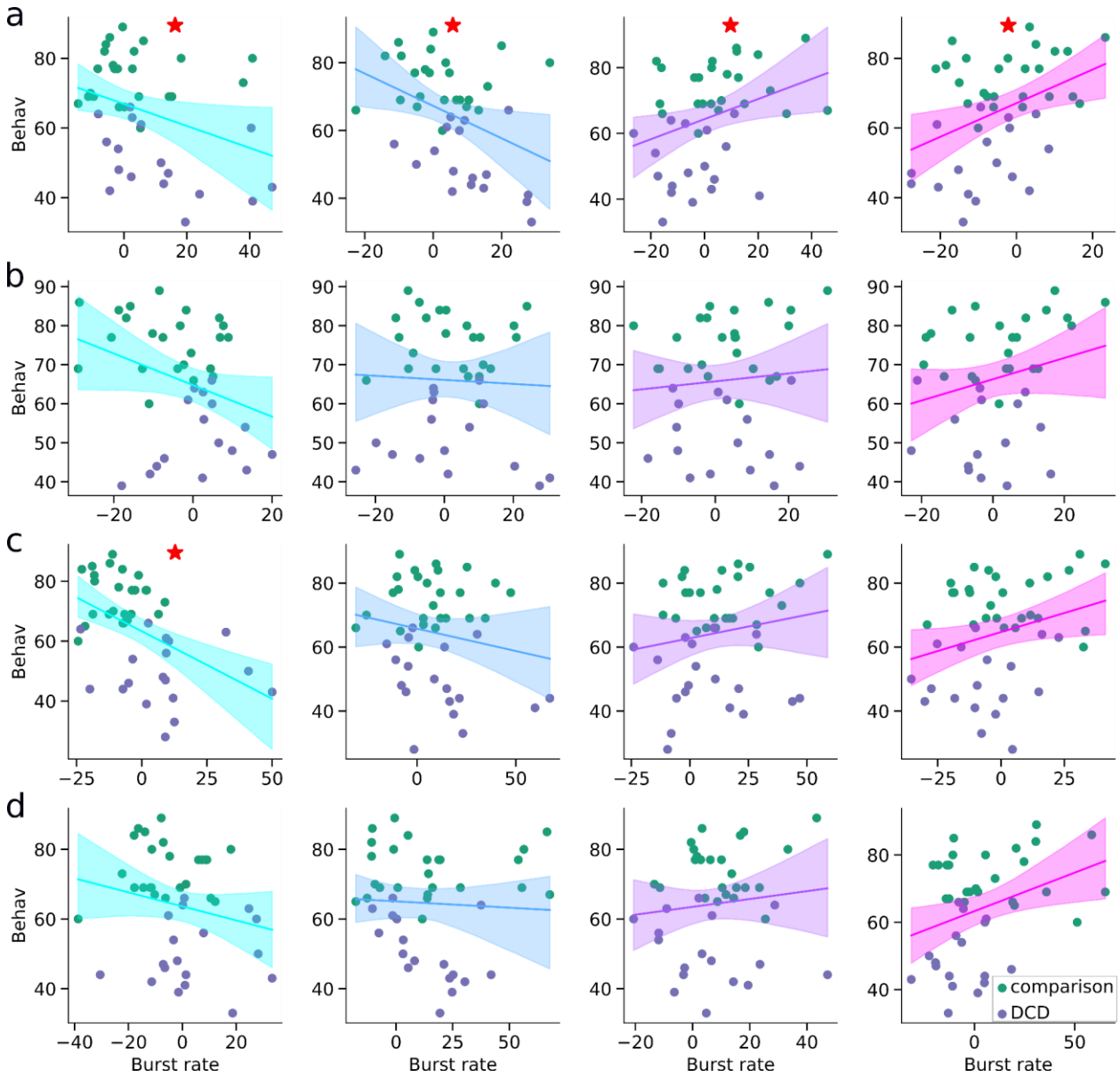

Figure 5. Waveform-specific burst rates along PC7 have consistent relationships with motor skill. a) Relationship between the mean burst rate of bursts from with a score within the (from left to right) first, second, third, and fourth quartile of PC7 during the ObF condition and MABC 2 total score. b-d) As in a, for the ObG (b), ExF (c), and ExG (d) conditions. Dots represent individual subjects. Red stars indicate

significant correlations. Solid lines represent the results of linear regressions between burst rate and MABC 2 total score, and shaded regions denote bootstrapped 95% confidence intervals.

3.6 DCD is associated with altered hemispheric distribution of burst rates

Because the preceding analyses combined bursts across hemispheres, we next examined burst rates separately in the ipsilateral and contralateral hemispheres, as prior work has shown that waveform motifs can differ in their lateralized rate dynamics (Rayson et al., 2023). We therefore examined the rate of bursts in each quartile of PC7 in each condition, conditioned on whether they were detected in the hemisphere ipsi- or contra-lateral to each participant's dominant hand (Figure 6). This revealed a similar pattern of results in the ipsilateral hemisphere as the across-hemisphere analysis, with the DCD group having a higher rate of first quartile bursts and a lower rate of fourth quartile bursts across conditions (Table S2; Figure 6). The only difference observed in the contralateral hemisphere was in the first quartile during the ExF condition, which occurred at a higher rate in the DCD group compared to the comparison group (Table S2).

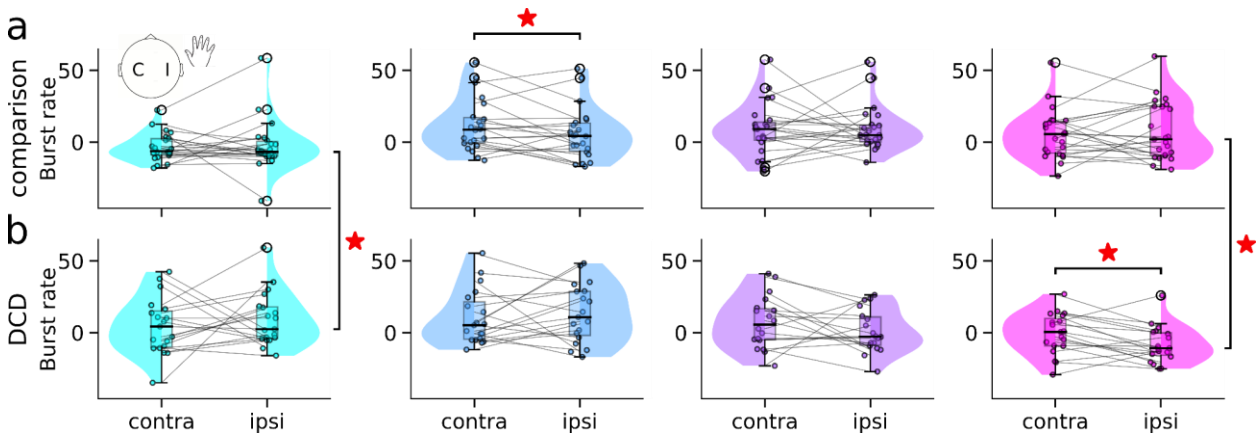

Figure 6. DCD subjects display hemispheric differences in waveform-specific burst rates along PC7. a) Mean burst rate for each hemisphere of the comparison group for the (from left to right) first, second, third, and fourth quartiles of PC7 over all conditions. Points represent individual subjects. Red stars indicate significant differences between groups or hemispheres. The inset shows the location of the analyzed bursts, relative to the dominant hand (C = contralateral, I = ipsilateral). b) As in a, for the DCD group.

As before, we followed up these permutation tests with a linear mixed model analysis of burst rate with group, hemisphere, and their interaction as fixed effects, and subject-specific intercepts and condition slopes as random effects. For the first quartile of PC7, there was a main effect of group ($\chi^2(1) = 9.37$, $p = 0.002$) and hemisphere ($\chi^2(1) = 4.19$, $p = 0.041$), with higher burst in the DCD group and slightly greater rates in the ipsilateral hemisphere overall. For the second quartile, we observed a significant group-by-hemisphere interaction ($\chi^2(1) = 7.66$, $p = 0.006$). In the comparison group, burst rates were significantly higher in the contralateral than ipsilateral hemisphere ($M_{contra} = 10.51$, $SD = 20.94$ %; $M_{ipsi} = 2.37$, $SD = 18.61$ %; $t(144) = 2.92$, $p = 0.004$). No hemispheric differences were observed in the DCD group ($t(146) = -1.05$, $p = 0.294$), though mean rates were slightly higher ipsilaterally ($M_{contra} = 9.09$, $SD = 23.47$ %; $M_{ipsi} = 11.58$, $SD =$

21.56 %). There were no effects of group, condition, or their interaction for the third quartile. The fourth quartile also showed a significant group-by-hemisphere interaction ($\chi^2(1) = 7.06$, $p = 0.008$). Burst rates in the ipsilateral hemisphere were significantly higher in the comparison group ($M_{DCD} = -9.45$, $SD = 15.58$ %; $M_{comparison} = 5.12$, $SD = 23.90$ %; $t(86.2) = -3.75$, $p < 0.001$), with no group difference in the contralateral hemisphere ($t(86.1) = -0.78$, $p = 0.436$). Within-group comparisons showed a significant hemisphere asymmetry in the DCD group ($M_{contra} = -1.83$, $SD = 18.05$ %; $t(147) = 2.59$, $p = 0.011$), but not in the comparison group ($t(145) = -1.12$, $p = 0.266$). Children with DCD thus exhibited either reduced or inverted asymmetry depending on the waveform motif, with group differences emerging most consistently in the ipsilateral hemisphere.

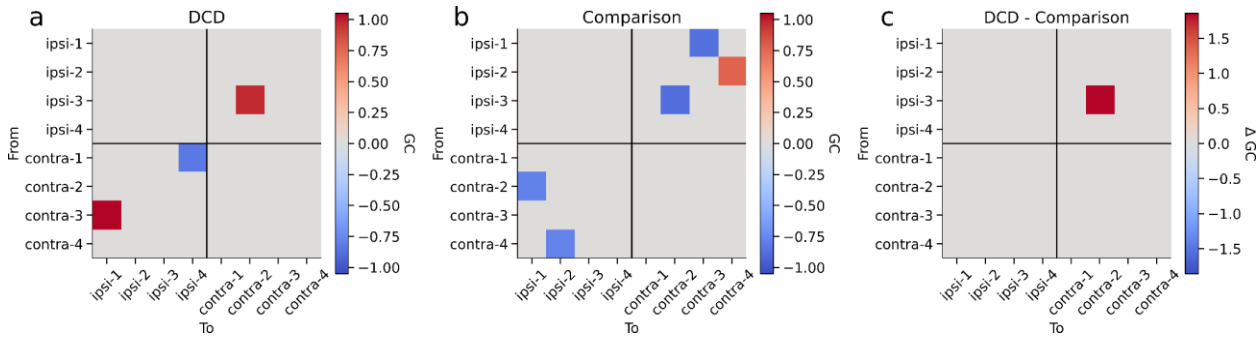

Figure 7. DCD subjects have greater functional connectivity between ipsi- and contra-lateral sensorimotor cortex during bursts of distinct waveform shapes. a) Significant granger causality between bursts in each quartile of PC7 in ipsi- and contra-lateral hemisphere sensorimotor cortex in the DCD group. Horizontal and vertical lines separate different regions. b) As in a, for the comparison group. c) Significant differences in Granger causality between groups (DCD minus comparison).

3.7 DCD participants exhibit reduced inter-hemispheric inhibitory functional connectivity during specific burst types

Given the hemispheric differences between groups in beta burst dynamics, we next examined whether the DCD group had altered functional interactions between ipsi- and contra-lateral sensorimotor cortex (relative to the dominant hand). We computed signed Granger causality between bursts of each quartile of PC7 in C3 and C4 using a negative binomial GLM framework (Kim et al., 2011; Agouram et al., 2025). Because our burst detection algorithm does not identify temporally overlapping bursts, within-hemisphere interactions are trivially inhibitory and were therefore excluded from analysis. In the comparison group, we observed significant recurrent interhemispheric connectivity for quartiles 2 and 4, as well as cross-quartile inhibition from first quartile ipsilateral bursts to third quartile contralateral bursts, third quartile ipsilateral bursts to second quartile contralateral bursts, and second quartile contralateral bursts to first quartile ipsilateral bursts (Figure 7a). In contrast, the DCD group showed markedly reduced interhemispheric inhibition, with only one significant inhibitory connection: from first quartile contralateral bursts to fourth quartile ipsilateral bursts, as well as two significant excitatory connections: one from third quartile ipsilateral bursts to second quartile

contralateral bursts, and one from third quartile contralateral bursts to first quartile ipsilateral bursts (Figure 7c). Permutation tests confirmed that inhibition was significantly lower in the DCD group for the connection from third quartile ipsilateral bursts to second quartile contralateral bursts (Figure 7c). DCD is therefore associated with reduced inhibitory, and in some cases reversed to excitatory, functional connectivity between sensorimotor hemispheres during specific beta burst types.

4. Discussion

This is the first study to apply waveform-based beta burst analyses to a neurodevelopmental condition, revealing differences not detectable with conventional time-frequency measures. Our findings demonstrate that children with DCD exhibit atypical beta burst dynamics, characterized by altered waveform-specific rate modulation and lateralization of burst rate dynamics during movement execution and observation. These alterations were especially evident for bursts with particular waveform motifs, suggesting that distinct types of beta bursts, which are increasingly recognized as functionally heterogeneous events (Rayson et al., 2023; Szul et al., 2023; Zich et al., 2023), are affected in the context of DCD. This extends prior observations that atypical beta power, brain connectivity, and hemispheric specialization are hallmarks of DCD (Brown-Lum and Zwicker, 2015; McLeod et al., 2016; Blais et al., 2018; Pranjić et al., 2024; Lum et al., 2025), and highlights waveform-specific beta bursts as a potential new lens through which to understand the neural bases of motor difficulties in neurodevelopmental conditions.

It has been suggested that different beta burst waveform motifs reflect different aspects of sensorimotor processing (Rayson et al., 2023; Szul et al., 2023). Our results support this model, revealing that children with DCD exhibited altered waveform-specific burst dynamics compared to a comparison group. Specifically, within the ipsilateral hemisphere, children with DCD showed increased rates of bursts characterized by one waveform motif (PC7 first quartile), and decreased rates of another motif (PC7 fourth quartile), suggesting disrupted interhemispheric organization. This was corroborated by the functional connectivity analysis, which revealed diminished inhibitory interactions between hemispheres in the DCD group compared to the comparison group. Notably, although no differences were found during action observation in previous work with infants (Rayson et al., 2023), the differences in beta burst rates found here were very similar during execution and observation. Altogether, these findings suggest that in DCD, specific burst waveform shapes provide markers of selective disruption in sensorimotor processes, possibly including the development of motor simulation mechanisms in childhood (Bieber et al., 2023; Keating et al., 2023).

If different beta burst motifs index distinct sensorimotor processes, then their atypical recruitment in DCD may help explain the difficulties in motor planning, execution,

and adaptation associated with the condition (Subara-Zukic et al., 2022), mirroring associations found between burst timing and both response time and error in healthy adults (Little et al., 2019). The ipsilateral increases and decreases in specific motifs observed in the DCD group may reflect atypical recruitment of sensorimotor circuits involved in internal models of both action execution and observation. Although we did not observe widespread lateralization effects in the comparison group, the altered pattern of inhibitory interhemispheric interactions in DCD suggests a possible disruption in the balance of excitation and inhibition across hemispheres. This pattern is consistent with resting-state fMRI findings of atypical interhemispheric connectivity and reduced hemispheric specialization in DCD (McLeod et al., 2014, 2016), which have been linked to differences in corpus callosum-mediated motor coordination (McLeod et al., 2016). According to the 'internal modeling deficit' (IMD) hypothesis, such disruptions can degrade predictive motor control and increase reliance on visual feedback (Subara-Zukic et al., 2022). If specific beta burst motifs contribute to internal modeling or interhemispheric calibration of motor commands, then their disrupted expression in DCD may underlie key features of the condition. Future studies should examine whether interventions targeting interhemispheric communication can restore typical burst motif dynamics and improve motor function.

Somewhat surprisingly, many group differences in burst rates were observed in the ipsilateral rather than contralateral hemisphere. This may seem counterintuitive, but it aligns with prior evidence that atypical interhemispheric cortical inhibition contributes to motor control difficulties in DCD (He et al., 2018). In particular, inhibitory control over the non-dominant hand appears selectively affected in DCD, suggesting atypical development of interhemispheric communication (Tallet et al., 2013). The observed differences in ipsilateral burst motif expression may therefore reflect difficulties with inhibiting motor output to the non-dominant hand, with consequences for motor planning, execution, and adaptation. Future work should test this hypothesis directly.

Our results were highly consistent across analyses, with group differences found almost exclusively along specific quartiles of a single principal component (PC7) for both observation and execution. A smaller effect in the execution conditions was also observed for PC8, suggesting that while most group differences were concentrated in one waveform dimension, additional motifs may also contribute. It is important to note that our PCA approach projects all bursts to all components, with each PC simply providing an unsupervised axis along which bursts are organized by waveform. While PCA does not involve traditional multiple comparisons correction, the fact that group differences were confined to PC7 (and marginally PC8), and showed a consistent pattern across analyses, suggests that these effects are unlikely to be spurious. Notably, PCs 7 and 8 were correlated with each other when the PCA analysis was run separately on the comparison and DCD groups (Figure 2f), suggesting that unsupervised PCA may not be the best

approach to characterize group differences. Future work could extend this approach using supervised dimensionality reduction techniques, such as generalized contrastive PCA (de Oliveira et al., 2025), to identify waveform features that most reliably distinguish between groups. While such methods may improve sensitivity, they are optimized for discrimination rather than interpretability, and additional analyses would be needed to link identified features to specific sensorimotor mechanisms.

Our study has several strengths, especially the inclusion of execution, observation, and non-biological motion (kaleidoscope) conditions. The non-biological motion baseline demonstrates that the effects are specific to sensorimotor processing, while the observation conditions show that these effects are not limited to motor execution, and perhaps extend to internal models engaged during both action execution and observation. Moreover, this is the first study to apply cutting-edge beta burst detection and waveform-based analysis methods in the context of neurodevelopmental conditions. However, several limitations should also be noted. First, our sample size, while comparable to previous EEG studies in DCD, was relatively modest, and future studies with larger cohorts will be important to replicate and extend these findings. Second, although we focused on central electrodes overlying sensorimotor regions, beta bursts in associative and prefrontal cortices may also contribute to motor planning and execution (Wessel, 2020; Diesburg et al., 2021; Liljefors et al., 2024). Third, because we used a block design to maximize power for mean burst rate comparisons, we were unable to examine fine-grained temporal dynamics of burst modulation within trials. Future studies using event-locked designs will be important to address this. Longitudinal studies will also be crucial for determining how disruptions in beta burst dynamics evolve across development and whether they predict longer-term motor outcomes across both neurotypical and neurodivergent development.

In conclusion, our findings reveal that disrupted sensorimotor beta burst dynamics in DCD are waveform-specific, supporting emerging models in which the functional heterogeneity of beta bursts plays a critical role in motor control. By identifying how different burst motifs are differentially affected in neurodevelopmental conditions, this work opens new avenues for understanding the neural mechanisms underlying atypical motor development and for developing burst-based biomarkers for early detection and intervention.

References

Agouram H, Szul MJ, Eusebio A, Daucé E, Sorrentino P, Bonaiuto JJ (2025) Beta Burst Waveform Motifs Link Cortico-Subcortical Connectivity and Clinical Improvement in Parkinson's Disease. :2025.07.09.25331208 Available at: https://www.medrxiv.org/content/10.1101/2025.07.09.25331208v1 [Accessed July 29, 2025].

Bates D, Mächler M, Bolker B, Walker S (2014) Fitting linear mixed-effects models using lme4. ArXiv Prepr ArXiv14065823.

Bieber E, Smits-Engelsman BC, Sgandurra G, Martini G, Guzzetta A, Cioni G, Feys H, Klingels K (2023) Insights on action observation and imitation abilities in children with Developmental Coordination Disorder and typically developing children. Res Dev Disabil 139:104556.

Blais M, Amarantini D, Albaret J, Chaix Y, Tallet J (2018) Atypical inter- hemispheric communication correlates with altered motor inhibition during learning of a new bimanual coordination pattern in developmental coordination disorder. Dev Sci 21:e12563.

Bo J, Lee C-M (2013) Motor skill learning in children with Developmental Coordination Disorder. Res Dev Disabil 34:2047–2055.

Bonaiuto J, Little S, Neymotin SA, Jones SR, Barnes GR, Bestmann S (2021) Laminar dynamics of high amplitude beta bursts in human motor cortex. NeuroImage 242:118479.

Boto E, Shah V, Hill RM, Rhodes N, Osborne J, Doyle C, Holmes N, Rea M, Leggett J, Bowtell R, Brookes MJ (2022) Triaxial detection of the neuromagnetic field using optically-pumped magnetometry: feasibility and application in children. NeuroImage 252:119027.

Brady B, Bardouille T (2022) Periodic/Aperiodic parameterization of transient oscillations (PAPTO)–Implications for healthy ageing. NeuroImage 251:118974.

Brown-Lum M, Izadi-Najafabadi S, Oberlander TF, Rauscher A, Zwicker JG (2020) Differences in White Matter Microstructure Among Children With Developmental Coordination Disorder. JAMA Netw Open 3:e201184–e201184.

Brown-Lum M, Zwicker JG (2015) Brain Imaging Increases Our Understanding of Developmental Coordination Disorder: a Review of Literature and Future Directions. Curr Dev Disord Rep 2:131–140.

Cheyne D, Jobst C, Tesan G, Crain S, Johnson B (2014) Movement-related neuromagnetic fields in preschool age children. Hum Brain Mapp 35:4858–4875.

de Cheveigné A (2020) ZapLine: A simple and effective method to remove power line artifacts. NeuroImage 207:116356.

de Oliveira EF, Garg P, Hjerling-Leffler J, Batista-Brito R, Sjulson L (2025) Identifying patterns differing between high-dimensional datasets with generalized contrastive PCA. PLOS Comput Biol 21:e1012747.

Debnath R, Buzzell GA, Morales S, Bowers ME, Leach SC, Fox NA (2020) The Maryland analysis of developmental EEG (MADE) pipeline. Psychophysiology 57:e13580.

Delorme A, Makeig S (2004) EEGLAB: an open source toolbox for analysis of single-trial EEG dynamics including independent component analysis. J Neurosci Methods 134:9–21.

Diesburg DA, Greenlee JD, Wessel JR (2021) Cortico-subcortical β burst dynamics underlying movement cancellation in humans. elife 10:e70270.

Donoghue T, Haller M, Peterson EJ, Varma P, Sebastian P, Gao R, Noto T, Lara AH, Wallis JD, Knight RT, Shestyuk A, Voytek B (2020) Parameterizing neural power spectra into periodic and aperiodic components. Nat Neurosci 23:1655–1665.

Drew AR, Quandt LC, Marshall PJ (2015) Visual influences on sensorimotor EEG responses during observation of hand actions. Brain Res 1597:119–128.

Feingold J, Gibson DJ, DePasquale B, Graybiel AM (2015) Bursts of beta oscillation differentiate postperformance activity in the striatum and motor cortex of monkeys performing movement tasks. Proc Natl Acad Sci U S A 112:13687–13692.

Fox J, Weisberg S, Price B, Adler D, Bates D, Baud-Bovy G, Bolker B (2019) car: Companion to Applied Regression. R package version 3.0-2. Website HttpsCRAN R-Proj Orgpackage Car Accessed 17 March 2020.

French B, Sycamore NJ, McGlashan HL, Blanchard CC, Holmes NP (2018) Ceiling effects in the Movement Assessment Battery for Children-2 (MABC-2) suggest that non-parametric scoring methods are required. PLoS One 13:e0198426.

Fu Y, Franz EA (2014) Viewer perspective in the mirroring of actions. Exp Brain Res 232:3665–3674.

Gaetz W, MacDonald M, Cheyne D, Snead OC (2010) Neuromagnetic imaging of movement-related cortical oscillations in children and adults: Age predicts post-movement beta rebound. NeuroImage 51:792–807.

He JL, Fuelscher I, Coxon J, Barhoun P, Parmar D, Enticott PG, Hyde C (2018) Impaired motor inhibition in developmental coordination disorder. Brain Cogn 127:23–33.

Henderson SE, Sugden D, Barnett AL (1992) Movement assessment battery for children-2. Res Dev Disabil Available at: https://psycnet.apa.org/doiLanding?doi=10.1037/t55281-000 [Accessed September 23, 2025].

Henderson SE, Sugden DA, Barnett AL (2007) Movement assessment battery for children, 2nd ed. London, UK: The Psychological Corporation.

Hobson HM, Bishop DV (2016) Mu suppression–a good measure of the human mirror neuron system? Cortex J Devoted Study Nerv Syst Behav 82:290.

Jackson PL, Meltzoff AN, Decety J (2006) Neural circuits involved in imitation and perspective-taking. Neuroimage 31:429–439.

Jeannerod M (2001) Neural Simulation of Action: A Unifying Mechanism for Motor Cognition. NeuroImage 14:S103–S109.

Jones SR (2016) When brain rhythms aren't 'rhythmic': implication for their mechanisms and meaning. Curr Opin Neurobiol 40:72–80.

Keating J, Gerson SA, Jones CRG, Vanderwert RE, Purcell C (2023) Possible disrupted biological movement processing in Developmental Coordination Disorder. Cortex 168:1–13.

Kim S, Putrino D, Ghosh S, Brown EN (2011) A Granger Causality Measure for Point Process Models of Ensemble Neural Spiking Activity. PLOS Comput Biol 7:e1001110.

Kumaravel VP, Farella E, Parise E, Buiatti M (2022) NEAR: An artifact removal pipeline for human newborn EEG data. Dev Cogn Neurosci 54:101068.

Leach SC, Morales S, Bowers ME, Buzzell GA, Debnath R, Beall D, Fox NA (2020) Adjusting ADJUST: Optimizing the ADJUST algorithm for pediatric data using geodesic nets. Psychophysiology 57:e13566.

Lenth R, Buerkner P, Herve M, Love J, Riebl H, Singmann H (2020) emmeans: estimated marginal means, aka least-squares means, v1. 5.1. Vienna R Core Team.

Liljefors J, Almeida R, Rane G, Lundström JN, Herman P, Lundqvist M (2024) Distinct functions for beta and alpha bursts in gating of human working memory. Nat Commun 15:8950.

Little S, Bonaiuto J, Barnes G, Bestmann S (2019) Human motor cortical beta bursts relate to movement planning and response errors. PLOS Biol 17:e3000479.

Lum JAG, Hamilton KM, Leow L-A, Marinovic W, Fuelscher I, Barhoun P, Ford TC, Hill AT, Nahravani S, Kirkovski M, Enticott PG, Hyde C (2025) Atypical Beta Oscillatory Dynamics Are Related to Poor Procedural Learning in Children With Developmental Coordination Disorder. Dev Sci 28:e70031.

McLeod KR, Langevin LM, Dewey D, Goodyear BG (2016) Atypical within-and between-hemisphere motor network functional connections in children with developmental coordination disorder and attention-deficit/hyperactivity disorder. NeuroImage Clin 12:157–164.

McLeod KR, Langevin LM, Goodyear BG, Dewey D (2014) Functional connectivity of neural motor networks is disrupted in children with developmental coordination disorder and attention-deficit/hyperactivity disorder. NeuroImage Clin 4:566–575.

Moca VV, Bârzan H, Nagy-Dăbâcan A, Mureșan RC (2021) Time-frequency super-resolution with superlets. Nat Commun 12:337.

Mognon A, Jovicich J, Bruzzone L, Buiatti M (2011) ADJUST: An automatic EEG artifact detector based on the joint use of spatial and temporal features. Psychophysiology 48:229–240.

Pedregosa F, Varoquaux G, Gramfort A, Michel V, Thirion B, Grisel O, Blondel M, Prettenhofer P, Weiss R, Dubourg V (2011) Scikit-learn: Machine learning in Python. J Mach Learn Res 12:2825–2830.

Pfurtscheller G (1981) Central beta rhythm during sensorimotor activities in man. Electroencephalogr Clin Neurophysiol 51:253–264.

Pfurtscheller G, Stancák A, Neuper C (1996) Post-movement beta synchronization. A correlate of an idling motor area? Electroencephalogr Clin Neurophysiol 98:281–293.

Pranjić M, Leung J, Tam KL, Polatajko H, Welsh T, Chau T, Thaut M (2024) Children with developmental coordination disorder display atypical interhemispheric connectivity during conscious and subconscious rhythmic auditory-motor synchronization. Sci Rep 14:19954.

Press C, Cook J, Blakemore S-J, Kilner J (2011) Dynamic Modulation of Human Motor Activity When Observing Actions. J Neurosci 31:2792–2800.

Querne L, Berquin P, Vernier-Hauvette M-P, Fall S, Deltour L, Meyer M-E, de Marco G (2008) Dysfunction of the attentional brain network in children with Developmental Coordination Disorder: A fMRI study. Brain Res 1244:89–102.

R Core Team (2022) R: A language and environment for statistical computing. Vienna, Austria: R Foundation for Statistical Computing.

Rayson H, Debnath R, Alavizadeh S, Fox N, Ferrari PF, Bonaiuto JJ (2022) Detection and analysis of cortical beta bursts in developmental EEG data. Dev Cogn Neurosci 54:101069.

Rayson H, Szul MJ, El-Khoueiry P, Debnath R, Gautier-Martins M, Ferrari PF, Fox N, Bonaiuto JJ (2023) Bursting with potential: How sensorimotor beta bursts develop from infancy to adulthood. J Neurosci Available at: https://www.jneurosci.org/content/early/2023/10/13/JNEUROSCI.0886-23.2023 [Accessed November 18, 2023].

Rier L, Rhodes N, Pakenham DO, Boto E, Holmes N, Hill RM, Reina Rivero G, Shah V, Doyle C, Osborne J, Bowtell RW, Taylor M, Brookes MJ (2024) Tracking the neurodevelopmental trajectory of beta band oscillations with optically pumped magnetometer-based magnetoencephalography Luo H, Colgin LL, eds. eLife 13:RP94561.

Sherman MA, Lee S, Law R, Haegens S, Thorn CA, Hämäläinen MS, Moore CI, Jones SR (2016) Neural mechanisms of transient neocortical beta rhythms: Converging evidence from humans, computational modeling, monkeys, and mice. Proc Natl Acad Sci 113:E4885–E4894.

Shin H, Law R, Tsutsui S, Moore CI, Jones SR (2017) The rate of transient beta frequency events predicts behavior across tasks and species. eLife 6 Available at: http://www.ncbi.nlm.nih.gov/pubmed/29106374 [Accessed February 7, 2019].

Subara-Zukic E, Cole MH, McGuckian TB, Steenbergen B, Green D, Smits-Engelsman BC, Lust JM, Abdollahipour R, Domellöf E, Deconinck FJ (2022) Behavioral and neuroimaging research on developmental coordination disorder (DCD): A combined systematic review and meta-analysis of recent findings. Front Psychol 13:809455.

Sugden DA (2006) Development Coordination Disorder as a specific learning difficulty. Leeds Consens Statement ESRC:2004–2005.

Szul MJ, Papadopoulos S, Alavizadeh S, Daligaut S, Schwartz D, Mattout J, Bonaiuto JJ (2023) Diverse beta burst waveform motifs characterize movement-related cortical dynamics. Prog Neurobiol 228:102490.

Tallet J, Albaret J-M, Barral J (2013) Developmental changes in lateralized inhibition of symmetric movements in children with and without Developmental Coordination Disorder. Res Dev Disabil 34:2523–2532.

Van Dyck D, Deconinck N, Aeby A, Baijot S, Coquelet N, Trotta N, Rovai A, Goldman S, Urbain C, Wens V (2022) Atypical resting-state functional brain connectivity in children with developmental coordination disorder. NeuroImage Clin 33:102928.

Veale JF (2014) Edinburgh Handedness Inventory – Short Form: A revised version based on confirmatory factor analysis. Laterality Asymmetries Body Brain Cogn 19:164–177.

Vieira VM (2012) Permutation tests to estimate significances on Principal Components Analysis. Comput Ecol Softw 2:103.

Weschler D (2011) WASI-II: Wechsler abbreviated scale of intelligence–second edition.

Wessel JR (2020) β-bursts reveal the trial-to-trial dynamics of movement initiation and cancellation. J Neurosci 40:411–423.

West TO, Duchet B, Farmer SF, Friston KJ, Cagnan H (2023) When do bursts matter in the primary motor cortex? Investigating changes in the intermittencies of beta rhythms associated with movement states. Prog Neurobiol 221:102397.

Wilkinson CL, Yankowitz LD, Chao JY, Gutiérrez R, Rhoades JL, Shinnar S, Purdon PL, Nelson CA (2024) Developmental trajectories of EEG aperiodic and periodic components in children 2–44 months of age. Nat Commun 15:5788.

Wilson PH, Smits- Engelsman B, Caeyenberghs K, Steenbergen B, Sugden D, Clark J, Mumford N, Blank R (2017) Cognitive and neuroimaging findings in developmental coordination disorder: new insights from a systematic review of recent research. Dev Med Child Neurol 59:1117–1129.

Wuang Y, Su C, Huang M (2012) Psychometric comparisons of three measures for assessing motor functions in preschoolers with intellectual disabilities. J Intellect Disabil Res 56:567–578.

Zich C, Quinn AJ, Bonaiuto JJ, O'Neill G, Mardell LC, Ward NS, Bestmann S (2023) Spatiotemporal organisation of human sensorimotor beta burst activity. Elife 12:e80160.

Supplementary Material

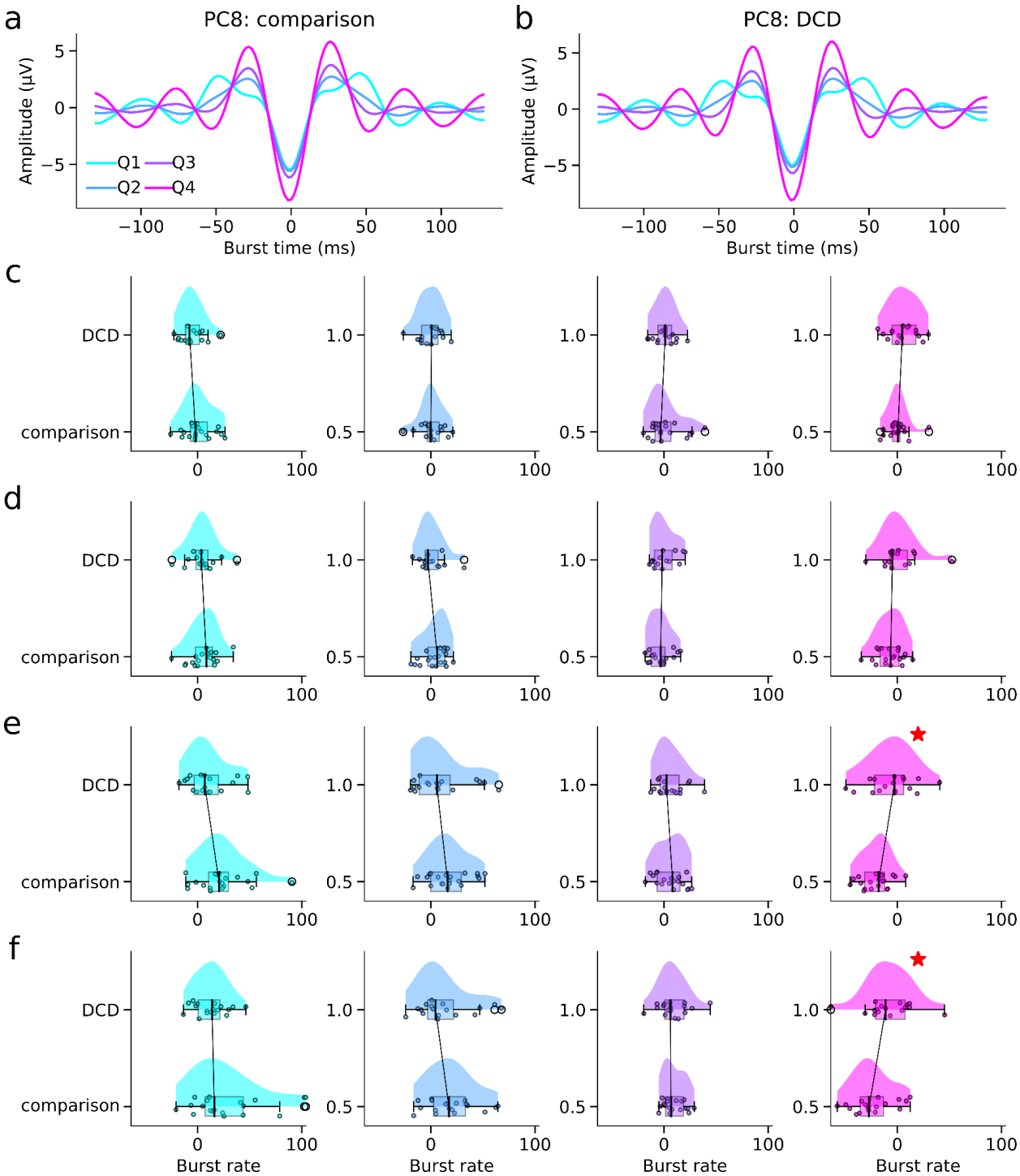

Figure S1. Comparison and DCD groups differ in terms of waveform-specific burst rates along PC8. a) Mean burst waveform shapes of bursts from the comparison group with a score within the first (cyan), second, third, and fourth (magenta) quartile of all burst scores for PC8. b) As in a, for bursts from the DCD group. e-g) Mean burst rate for each group for the (from left to right) first, second, third, and fourth quartiles

of PC8 during the ObF (c), ObG (d), ExF (e), and ExG (f) conditions. Points represent individual subjects. Solid lines link median values between groups. Red stars indicate significant differences between groups.

Table S1. Significant group differences in waveform-specific beta burst rates across principal component (PC) quartiles and conditions. For PCs and quartiles that showed significant burst waveform modulation (identified in Figure 3), the mean baseline-corrected burst rate (% change from baseline), standard deviation (SD), and between-group p-values (permutation test) for each condition (ObF, ObG, ExF, ExG).

PC	Quartile	Condition	$M_{comparison}$ (%)	$SD_{comparison}$ (%)	M_{DCD} (%)	SD_{DCD} (%)	*p*
7	1	ObG	-7.30	11.39	2.15	9.59	0.015
		ExF	-7.96	8.71	8.26	18.03	<0.001
		ExG	-5.65	11.01	4.23	15.90	0.039
	2	ObF	2.65	11.42	10.61	10.97	0.048
	3	ObF	4.75	13.55	-5.01	11.76	0.030
	4	ObF	-1.25	11.90	-9.37	10.51	0.042
		ExG	10.17	24.53	-6.83	12.28	0.015
8	4	ExF	-20.14	13.61	-5.79	22.29	0.025
		ExG	-23.38	19.37	-7.99	22.93	0.044

Table S2. Significant group differences in hemisphere-specific burst rates along PC7. Mean baseline-corrected burst rate (% change from baseline) and standard deviation (SD) are reported separately for the contralateral and ipsilateral hemispheres, for each quartile of PC7 and each condition (ObF, ObG, ExF, ExG).

Hemisphere	Quartile	Condition	$M_{comparison}$ (%)	$SD_{comparison}$ (%)	M_{DCD} (%)	SD_{DCD} (%)	*p*
ipsi	1	ObG	-7.26	18.91	6.00	10.43	0.020

		ExF	-6.73	13.31	10.05	19.52	0.004
		ExG	-9.60	12.65	7.05	25.99	0.019
	2	ObF	-5.01	16.37	9.50	11.94	0.006
	3	ObF	3.33	16.49	-11.29	16.91	0.016
	4	ObF	-0.76	13.41	-10.49	6.65	0.014
		ExF	3.04	23.74	-12.47	19.97	0.042
		ExG	12.51	28.71	-12.60	14.27	0.002
contra	4	ExF	-10.96	12.07	4.71	24.53	0.018